# Effect of wall boundary on the scrape-off layer losses of high harmonic fast wave in NSTX and NSTX-U

Eun-Hwa Kim ⓘD, Nicola Bertelli ⓘD, Masayuki Ono ⓘD, Ernest J. Valeo, Joel C. Hosea, and Rory J. Perkins ⓘD

View Online    Export Citation    CrossMark

## ARTICLES YOU MAY BE INTERESTED IN

# Effect of wall boundary on the scrape-off layer losses of high harmonic fast wave in NSTX and NSTX-U

View Online    Export Citation    CrossMark

Eun-Hwa Kim,[a] (iD) Nicola Bertelli, (iD) Masayuki Ono, (iD) Ernest J. Valeo, Joel C. Hosea,[b] and Rory J. Perkins (iD)

## AFFILIATIONS

Princeton Plasma Physics Laboratory, Princeton, New Jersey 08543, USA

[a] Electronic mail: ehkim@pppl.gov
[b] Deceased.

## ABSTRACT

We perform numerical simulations of high harmonic fast waves (HHFWs) in the scrape-off-layer (SOL) of National Spherical Torus Experiment (NSTX)/NSTX-U using a recently developed 2D full wave code. We particularly show that a realistic NSTX SOL boundary can significantly affect HHFW propagation and power losses in the SOL. In NSTX SOL boundaries, HHFW is easily localized near the antenna and propagates less to the SOL, and thus, less power is lost to the SOL. We also show that the lower SOL power losses occur when the SOL volume is smaller and the distance between the last closed flux surface and the antenna is shorter. We investigate the effect of electron density in front of the antenna and the ambient magnetic field strengths on the SOL power losses as well. Showing consistency with the experiments, SOL losses are minimized when the SOL density is near the critical density where the fast wave cutoff is open, and the plasma is strongly magnetized.

*Published under license by AIP Publishing.* https://doi.org/10.1063/1.5091579

## I. INTRODUCTION

Radio frequency (RF) heating and current drive are essential components in many magnetic fusion devices. Understanding of the interaction between RF antennas and the scrape-off layer (SOL), the region of the plasma between the last closed flux surface (LCFS) and the SOL boundary, is critical to optimize performance of RF in a tokamak because a significant fraction of the RF wave power can be lost in the SOL instead of being delivered to the core plasma as desired.[1–6] The SOL RF power loss is expected to play an increasingly important role in future higher power RF experiments including that in ITER. Since the SOL plasma is essentially "cold" from the RF wave physics point of view, the present analysis should be applicable, for example, to ITER ICRF experiments especially during the initial lower field operations.

Experimental and theoretical studies of the high harmonic fast wave (HHFW) on the National Spherical Torus Experiment (NSTX)[7,8] have been focused on optimizing core heating and CD efficiency by minimizing power losses in the SOL.[9] The experiments showed that the HHFW core heating efficiency in NSTX strongly depends on the ambient magnetic field strength. For instance, estimated core heating efficiency from the NSTX experiments increases

from 44% to 65% by increasing the magnetic field from 0.45 to 0.55 T.[1,2] Heating efficiency is also found to be sensitive to the electron density in the SOL. Because the HHFW has frequency much higher than the local fundamental ion cyclotron frequency and much lower than the local lower hybrid frequency, this wave propagation begins when the local density exceeds the critical density ($n_{ec}$) satisfying the fast wave (FW) cutoff condition $N_{\parallel}^2 = \mathcal{R}$, where $N_{\parallel}$ is the refractive index parallel to the ambient magnetic field and $\mathcal{R}$ is the Stix notation,[10] respectively. One can also show that $n_{ec} \propto n_{\parallel}^2 \omega B_T$,[2,3] where $\omega$ is the wave angular frequency and $B_T$ is a magnetic field, respectively, and higher core heating occurs[2,3] when the density in front of the antenna ($n_{ant}$) is below $n_{ec}$, thereby the HHFW is evanescent in the SOL which suggests reduction in the SOL RF power loss.

A number of power loss mechanisms in the SOL have been proposed including collisional losses,[11] surface wave propagation associated with large poloidal wave numbers,[11] antenna reactive field losses,[2] and RF sheath dissipation;[12–14] however, it is not well investigated which is the dominant mechanism of the power losses. There are several numerical efforts[18,19] to understand power losses of HHFW in the SOL of the NSTX/NSTX-Upgrade[16] using all order spectral algorithm (AORSA) full-wave code.[15] They have inserted into AORSA, an

artificial "collisional" damping mechanism as a proxy to represent the actual unknown mechanism(s) in order to understand whether the large wave electric field amplitude is one of the main drivers of the SOL power losses. They showed that power losses in the SOL start to significantly increase when evanescent HHFW begins propagating in the SOL due to higher $n_{ant}$, which is consistent with the experiments. They also showed that strong RF wave amplitude with the standing mode structure in the SOL leads strong power losses.

Because the power lost to the SOL scales with the amplitude of the RF field[18,19] and the volume of the SOL region which supports the RF fields, understanding wave structure and amplitude in a realistic SOL boundary is essential for investigating the power loss mechanisms in the SOL of a tokamak. However, for simplicity, the initial AORSA investigation adopted idealized rectangular boundaries, which are significantly larger than the actual NSTX SOL boundary.

In this paper, we investigate the HHFW structure in the SOL by adopting realistic vacuum vessel boundaries and examine the trend SOL loss along the SOL size, plasma density, and/or the magnetic field strength. We thus utilize a recently developed two dimensional full-wave (FW2D) code. The FW2D code can easily adopt various SOL boundaries because this code uses the finite element method and an unstructured triangular mesh. The FW2D code solves cold plasma equations and has been originally developed to examine plasma waves in space plasma. Since a cold plasma approximation is adequate to determine wave behavior in space,[20] this model has been used to examine low frequency waves near the ion cyclotron frequency in the planetary magnetospheres.[21–23] More recently, this has also been successfully adopted to the tokamak geometry.[23] The FW2D code is ideal for investigating waves in the SOL plasma because realistic 2D SOL boundary shapes and arbitrary density profiles can be adopted in the code, and the SOL plasma can be well described by a cold plasma for the present wave physics study.

The present paper is structured as follows: A brief description of the FW2D code is in Sec. II. A collisional effect is shown in Sec. II A. In Sec. II B, we performed benchmarking of the FW2D with the AORSA using the same rectangular SOL boundary condition and demonstrated that both codes yielded essentially the same SOL wave patterns and the losses. We demonstrate the effects of the SOL boundary on the SOL losses by adopting rectangular and hexagonal boundaries in Sec. III. In Sec. IV, we investigate the effects of the SOL size, density in front of the antenna, and magnetic field on HHFW power losses. Section V contains a summary and discussion.

## II. FW2D MODEL DESCRIPTION

A finite element full wave code, termed FW2D, appropriate for general geometries and boundaries has been developed.[21,23] The code currently solves the cold plasma full wave equations in two dimensions. Assuming time dependence, $\exp(-i\omega t)$, the linear and cold plasma wave equation takes the form

$$\nabla \times (\nabla \times \mathbf{E}) - \left(\frac{\omega}{c}\right)^2 \epsilon \cdot \mathbf{E} = 4\pi i \frac{\omega}{c^2} \mathbf{J}_{ext}, \qquad (1)$$

where $\mathbf{E}$ is the perturbed electric field, $\omega = 2\pi f$ is the wave angular frequency, $c$ is the light speed, $\epsilon$ is the cold plasma dielectric tensor, and $\mathbf{J}_{ext}$ is the external current source representing the antenna.

The dielectric tensor $\epsilon$ is expressed in coordinates aligned along and across the local ambient magnetic field direction $\hat{\mathbf{b}} \equiv \mathbf{B}_0/|\mathbf{B}_0|$, where $\mathbf{B}_0$ is an ambient magnetic field. For an axisymmetric plasma

model, Eq. (1) can be expressed in cylindrical $(r, z, \phi)$ coordinates and all variables are represented as a superposition of Fourier modes with dependence $\exp(in_\phi\phi)$, where $n_\phi$ is the toroidal wave number.

The electric field $\mathbf{E}$ is represented in terms of its projections along $(\hat{b})$ and perpendicular $(\hat{\xi}, \hat{\eta})$ to $\mathbf{B}_0$, where $\hat{\xi} \equiv \hat{r} \times \hat{b}$ and $\hat{\eta} \equiv \hat{b} \times \hat{\xi}$. Thus, the electric field can be described to

$$\mathbf{E}(r,z) = \sum_{n_\phi} \left( E_b \hat{b} + E_\eta \hat{\eta} + E_\xi \hat{\xi} \right) \exp(in_\phi\phi). \qquad (2)$$

Equation (1) has been solved on an unstructured triangular mesh. We represent the variation of the electric field within each triangle by vertex-based linear finite elements local basis function, $F_{j,k}$, where $j$ labels each triangle and $k = 1, 2, 3$ labels each of its vertices. The $F_{j,k}$ varies linearly between 1 at the $k$th vertex and 0 at the other vertices, and is identically 0 outside triangle $j$, thus the electric field is

$$E = \sum_{j,k} E_{j,k} F_{j,k}. \qquad (3)$$

Then, Eq. (1) is cast into the matrix form by taking its inner product in turn with each $F_{j,k}$ and integrating by parts to obtain the weak variational form (see, for example, Ref. 24)

$$\int d\phi r dr dz \left\{ (\nabla \times \mathbf{F}_{j,k}^*) \cdot (\nabla \times \mathbf{E}) + \mathbf{F}_{j,k}^* \cdot \epsilon \cdot \mathbf{E} + i4\pi \frac{\omega}{c^2} \mathbf{F}_{j,k}^* \cdot \mathbf{J}_{ext} \right\} = 0. \qquad (4)$$

Substitution of Eq. (3) into Eq. (4) yields a sparse matrix system that is amenable to solution by standard algorithms. To take advantage of the sparseness of the matrix system, we employed a Gibbs algorithm[25] to reorder the mesh to minimize the bandwidth of the matrix.

The density of the mesh can be specified based on the expected wavelength obtained from solution of the local dispersion (except close to resonances) so that the most efficient resolution can be used. We generated the mesh by using an adoption of DISTMESH[26] or TRIANGLE[27] algorithms that construct 2D triangle meshes for given specific boundaries and target density function. These mesh algorithms are particularly useful because they allow us to pack the extra resolution where waves propagate with the short wavelength and the complex SOL boundary (see Fig. 2 of Ref. 22).

Some advantages of using the finite element method and unstructured triangular mesh are that the employed local basis functions can be readily adapted to curving SOL boundary shapes, and the computational time is short. Thus, the FW2D code is well suited to investigate wave properties in realistic SOL boundaries. Figure 1 shows examples of the mesh generated using the TRIANGLE algorithm for the tokamak plasma, which adopts different boundary shapes. The first main plasma boundary as shown in Fig. 1(a) follows the LCFS, which has been used for previous simulations.[15,28] Because this boundary does not include the SOL, recent simulations extended the simulation domain from LCFS to larger rectangular SOL boundary,[18,19,29] which is similar to Fig. 1(b). However, the SOL in this boundary is much larger than the realistic SOL boundary as shown in Fig. 1(c). We will adopt different size of rectangular and actual experimental SOL boundaries and examine wave structures in the SOL.

The FW2D code has successfully examined waves in space plasmas. In order to describe open space, previous simulations in planetary magnetospheres have adopted the absorbing boundary condition by
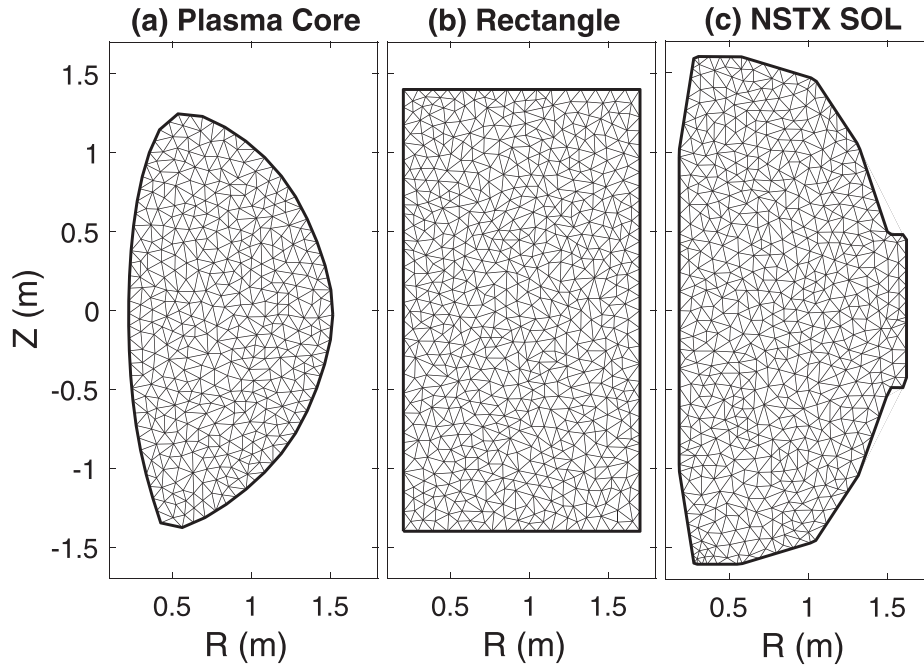
**FIG. 1.** Examples of the unstructured triangle mesh from the TRIANGLE algorithm using (a) the last closed flux surface, (b) rectangular, and (c) NSTX SOL boundaries.

adding strong collisions near the boundaries.[21–23] In the FW2D code, a collisional frequency ($\nu$) can be implemented in the momentum equation, and then, the plasma ($\omega_p$) and cyclotron ($\omega_c$) frequencies can be replaced with

$$\omega_p^2(\omega_c) \rightarrow \frac{\omega_p^2(\omega_c)}{1 + i\nu/\omega}. \qquad (5)$$

The collisions can be added in the simulation domain and near the SOL boundaries to represent an ad-hoc model for wave dissipation and/or absorption. In tokamak plasmas, the outer boundaries can be assumed to be perfectly reflecting to describe a metal wall.[18,19,30] Collisions can be included in order to represent an arbitrary loss mechanism[18] in both core and the edge plasma to absorb all incoming wave energy without requiring energy loss at the boundaries.

We should emphasize that the "collisionality" we are introducing here is a wave damping factor representing some type of wave energy dissipation mechanism which is at present unknown. The loss mechanism might be due to non-collisional in nature including the plasma sheath formation. Since the SOL is an open field line region, the power can be lost along the magnetic field lines into the plasma facing components (PFCs) by a number of loss mechanisms. In NSTX, we did indeed see such strong power flow along the magnetic field lines into the outer divertor PFCs which cannot be attributed to just collisional absorption.[5] Instead of actually trying to simulate the experiment, we investigate here the trend of SOL loss as those experimentally relevant parameters such as the SOL width, SOL volume, SOL plasma density ($n_{ant}$), and $n_\phi$ and $B_T$ are varied for a given SOL wave dissipation rate represented by the "collisionality".

## A. Collisional effects

In this section, we show the relative insensitivity of the SOL wave fields and resulting losses to the core absorptions by adopting several

core collisional frequencies as shown in Fig. 2(a). The collision in the plasma core has been assumed to be $\nu_{core}(\rho_{pol}) = \nu_{core}^{max} \exp\left(-(\rho_{pol} - \rho_0)^2/\Delta\rho^2\right)$, where $\nu^{max}$ is the maximum value of $\nu_{core}$, $\nu_{core}^{max}/\omega$ = 0.05, 0.1, and 0.5, respectively, $\rho_{pol}$ is the square root of the normalized poloidal flux, $\rho_0 = 0.1$ is where $\nu = \nu_{core}^{max}$, and $\Delta\rho = 0.8$ is an arbitrary constant. The $\nu_{core}$ exponentially decreases near the LCFS as shown in Fig. 2(a), and the collision in the SOL is assumed to be $\nu_{SOL}/\omega = 0.01$.

We then perform simulations using single toroidal mode numbers, $n_\phi = -12$ or $-21$, which correspond to an NSTX antenna phase of $-90°$ or $-150°$, respectively, and various densities in front of the antenna ($n_{ant}$). The electron density in the SOL is assumed to be exponentially decaying, which is the same as the one used in the previous simulations (see Fig. 1 of Ref. 18). The waves are launched with the wave frequency of $f = 30$ MHz at $R = 1.575$ m near the mid plane.

Figure 2(b) is the total electric fields in the rectangular SOL boundary for various collisions when we adopt $n_\phi = -12$ and the density in front of antenna $n_{ant} = 1 \times 10^{18}$ m$^{-3}$. In this figure, the dashed black and the solid red lines are the LCFS and the FW cutoff layer, respectively. We also plot the wave solution along the $Z$ direction at $R = 1.55$ m in Fig. 2(c). Here, the wave solutions in the plasma core are significantly different for increasing $\nu_{core}$. For $\nu_{core}^{max}/\omega = 0.05$, the ray path and wave reflection in the plasma core have been clearly seen, while for $\nu_{core}^{max}/\omega = 0.5$, wave energy is totally absorbed to the plasma as soon as the waves propagate into the plasma core. On the other hand, in spite of significant differences of wave propagation patterns in the plasma core for various collisions in the plasma core, waves in the SOL are almost identical.

The nearly identical wave structures in the SOL as shown in Fig. 2(c) confirm that the wave solutions in the SOL are almost independent to $\nu_{core}/\omega$ when $\nu_{core}/\omega$ is strong enough to absorb all incoming
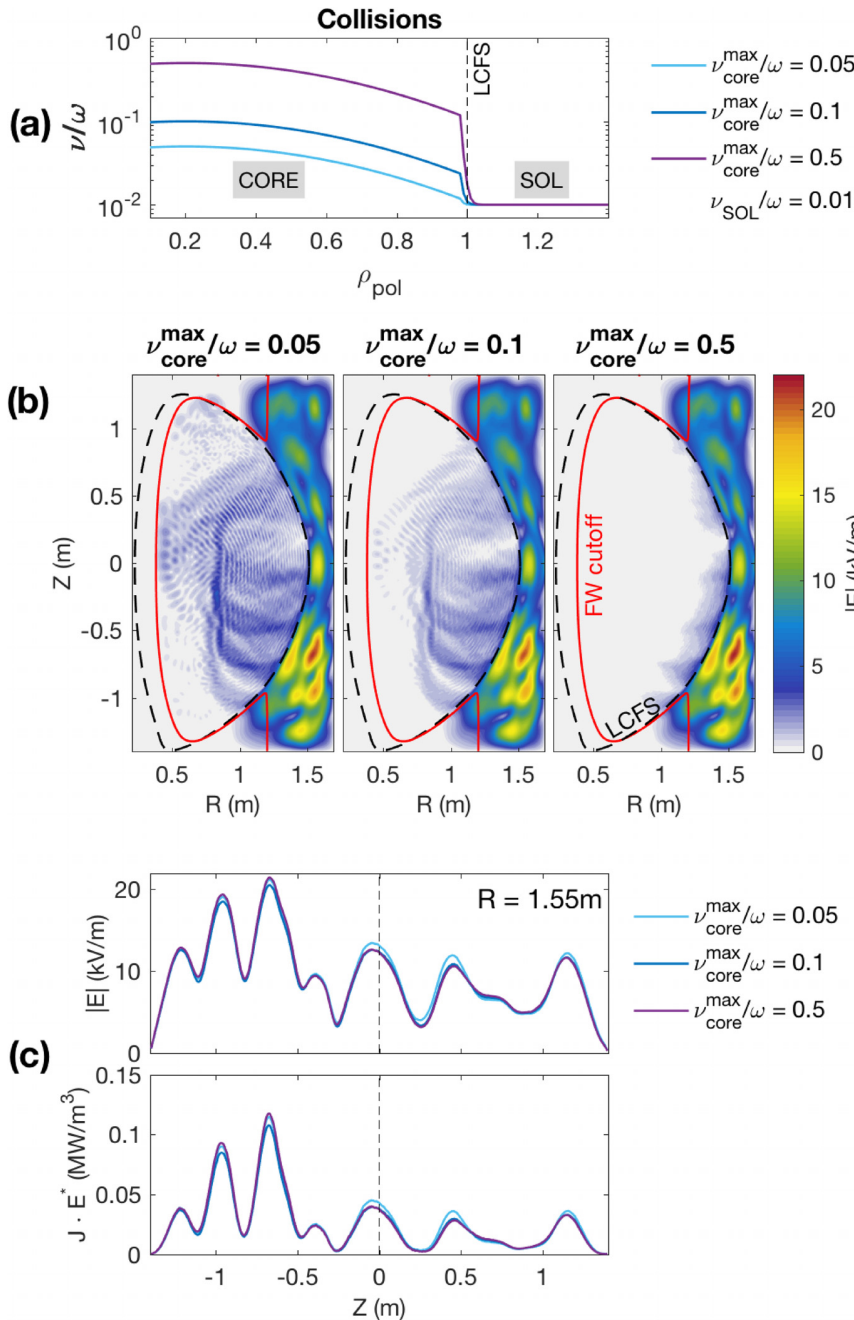
**FIG. 2.** (a) Adopted collisions that have the maximum values in the plasma core of (light blue) $\nu_{core}^{max}/\omega = 0.05$, (blue) 0.1, and (purple lines) 0.5. The collisions in the SOL are assumed to be $\nu_{SOL}/\omega = 0.01$. (b) Calculated total electric field amplitude from FW2D for $\nu_{core}^{max}/\omega = 0.05$, 0.1, and 0.5. The dashed black and solid red lines are the LCFS and the FW cutoff layer, respectively. (c) Total electric field amplitude and $\mathbf{J} \cdot \mathbf{E}^*$ along the $Z$ direction at $R = 1.55$ m for $\nu_{core}^{max}/\omega = 0.05$, 0.1, and 0.5.

wave into the plasma core, and waves in the plasma core do not affect waves in the SOL significantly.

## B. Comparison between FW2D and AORSA

In this section, we compare the results from FW2D with the existing full wave kinetic code AORSA for code benchmarking. The AORSA, which is valid to all order of Larmor radius and can resolve arbitrary ion cyclotron harmonics, is ideally suited to examine RF waves in the hot plasma core of tokamak.[15,17–19,30] We perform wave simulation benchmarking by adopting the same plasma conditions in the SOL that has been used in AORSA calculations,[18] such as SOL boundary shape and locations, magnetic equilibrium, electron density, and antenna location and direction in the SOL. A key difference between FW2D and AORSA is in the wave absorption model in the hot plasma core while the cold SOL plasma region is essentially the

same for the both codes. With arbitrary collisions in the plasma core, we perform FW2D wave simulations by adopting the same plasma conditions in the SOL that has been used in AORSA calculations.[18]

Both the codes adopt the perfect reflecting wave SOL boundary condition, implying no power dissipation at the reflecting boundary. To add dissipation to the SOL plasmas, both models employ collisional wave damping terms as noted above. In reality, the reflecting boundary has some level of dissipation. The SOL plasmas also have dissipation from actual collisions including those from neutral molecules and impurities. There are various possible SOL dissipation mechanisms as noted earlier. Since the SOL plasmas are by definition in the open field line region, the SOL plasma power flow to the nearby wall is also expected to be quite rapid. This relatively rapid power dissipation is modeled here by adopting relatively high values of collisional damping.

The comparison between FW2D and AORSA without collisions in the SOL is presented in Fig. 3. The plasma LCFS, antenna location, and boundaries are chosen to be the same. This figure shows total electric field amplitudes obtained by FW2D and AORSA codes for $n_\phi$ = −21 and $N_{ant} = 2 \times 10^{18}$ m$^{-3}$ in NSTX shot 130608. Here, simulation results from AORSA are reproduced from Ref. 18.

In spite of such differences in methodology between two codes, Fig. 3 shows that the simulations from FW2D and AORSA codes have excellent agreement with a similar standing wave phase and amplitude patterns in the SOL. The core wave structures are also quite similar between two codes cases. The apparent finer granularities observed in the FW2D wave field structure can be attributable to the somewhat finer mesh sizes and the triangular mesh of FW2D. The similarity of the core wave field structures is the fact that the fast wave propagation is reasonably well described by the cold plasma wave model. The vertical cross sections of wave electric fields are shown for R = 1.55 m and 1.65 m in Fig. 3(c). As can be seen from the figure, the wave electric field amplitudes are quite similar in amplitude and the phase for both radii.

The clear utilization of FW2D is that it is computationally much faster than the AORSA. For example, the FW2D code takes about
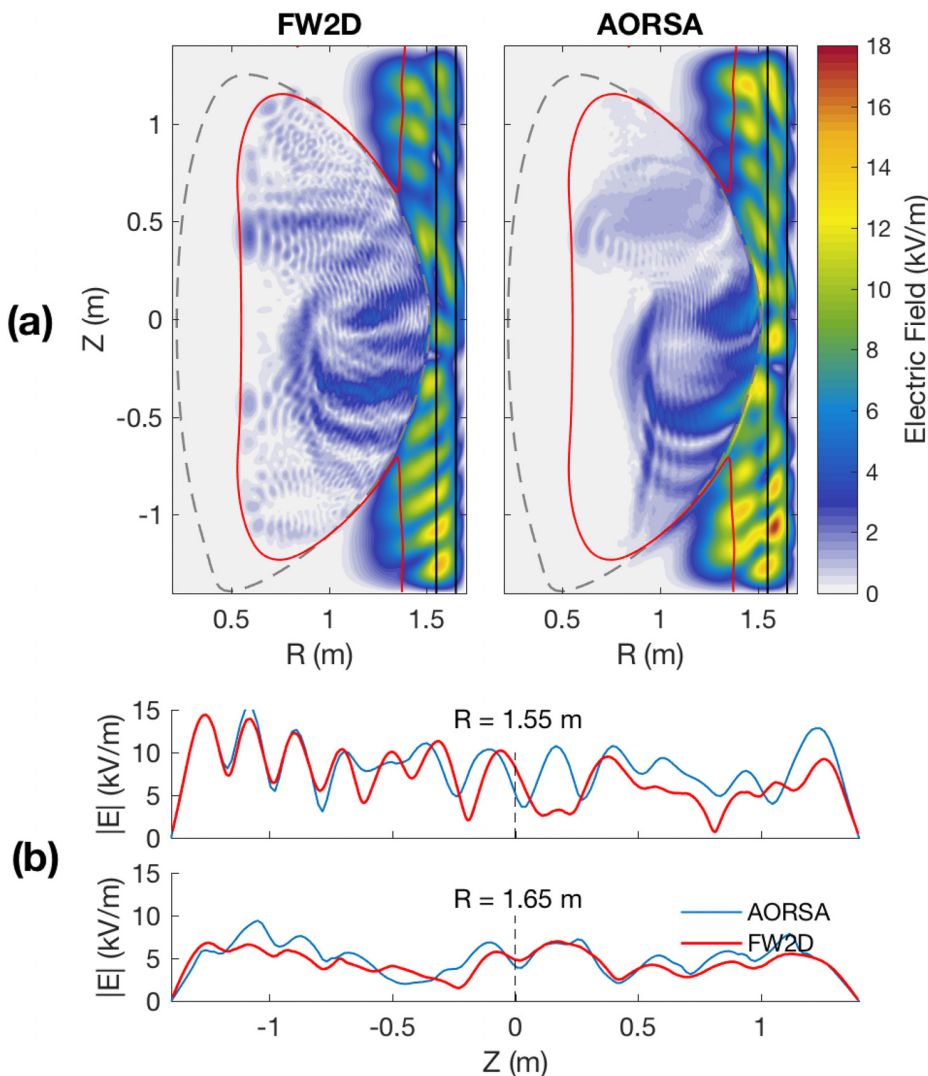


FIG. 3. (a) Total electric field amplitude in the NSTX shot 130608 using FW2D and AORSA codes for $n_{ant} = 1 \times 10^{18}$ m$^{-3}$ with the toroidal mode number $n_\phi = -21$ and (b) Total electric field amplitude along Z at R = 1.55 m and 1.65 m from (red) FW2D and (blue) AORSA codes.

10 min for the mesh number of $1 \times 10^5$ to get the results using only single CPU, a level manageable on a personal computer, while AORSA takes around 10 min using over 1000 processors for the resolution of $160 \times 160$, thus usually needs a much larger cluster. Therefore, the FW2D can efficiently provide the wave properties in the SOL and enables us to perform numerical surveys by adopting various plasma and more realistic SOL boundary conditions.

The comparison with the fully kinetic AORSA code and the previous core collisionality scan shows that the cold plasma full wave code FW2D is indeed well suited to investigate the SOL wave power loss mechanism. We may note that the present full core power absorption condition yields minimum levels of edge wave fields. If the core power absorption condition is not satisfied such as the case of multiple reflections, the SOL fields and resulting SOL power loss could be correspondingly larger. For the reminder of the paper, we investigate wave structures and power losses in the SOL for various conditions using FW2D with sufficiently strong absorption in the plasma core for simulations.

## III. EFFECT OF BOUNDARY SHAPE VARIATIONS

As shown in Fig. 1, the FW2D code can easily adopt various SOL boundary shapes. Prior to investigate wave properties in the actual NSTX SOL boundary, we explore wave properties in various idealized boundaries. Figure 4 shows boundaries that we used, such as rectangular boundaries of various sizes (light blue, blue, and purple), hexagonal (dark red), and NSTX SOL (black lines) boundaries.

Figure 5 shows the resulting total electric fields for (a) $n_\phi = -12$ and $n_{\text{ant}} = 1 \times 10^{18}$ m$^{-3}$ and (b) $n_\phi = -21$ and $n_{\text{ant}} = 2 \times 10^{18}$ m$^{-3}$
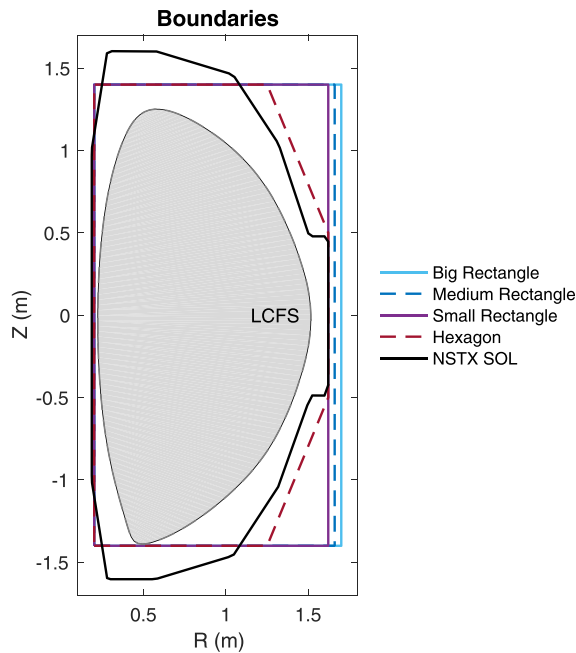


**FIG. 4.** Adopted boundaries in this paper; (light blue) big rectangular, (blue dashed) medium rectangular, (purple) small rectangular, (red dashed) hexagonal boundaries, and (thick black solid lines) NSTX boundary. The gray shaded region represents the plasma core, and the thin black line is the LCFS.

for the rectangular and hexagonal boundaries. In the first to the third columns (light blue to purple boundaries), the boundaries are rectangular, and the outer boundaries are shifted from $R = 1.7$ m to 1.62 m, thus the SOL volume is reduced. The standing mode structure becomes weaker with the SOL size reduction. For the smallest rectangular boundary in the third column in Fig. 5, the waves for $n_\phi = -12$ even start to be localized near the antenna. When we adopt a hexagonal SOL boundary as shown in the fourth column of Fig. 5, the wave structure near the antenna is similar to the smallest rectangular boundary in the third column showing reduced standing mode appearance due to the boundary shape.

We calculated fraction of power losses in the SOL in various boundaries. Because the FW2D code adopts a cold plasma approximation, power losses in the plasma core and SOL have been calculated by adopting collisions. Then, power losses in the SOL ($W_{\text{SOL}}$) and the plasma core ($W_{\text{core}}$) can be calculated as

$$W_{\text{SOL}} = \int_{\rho_{\text{pol}} > 1} \mathbf{J} \cdot \mathbf{E}^* dV \qquad (6)$$

and

$$W_{\text{core}} = \int_{\rho_{\text{pol}} \le 1} \mathbf{J} \cdot \mathbf{E}^* dV, \qquad (7)$$

where $V$ and $\mathbf{J}$ are the volume and the perturbed current density, respectively. Then, the fraction of power losses in the SOL ($P_{\text{abs}}$) can be defined as a ratio between total power absorbed to the plasma ($W_{\text{total}} = W_{\text{core}} + W_{\text{SOL}}$) to power loss in the SOL

$$\text{SOL power loss } (P_{\text{abs}}) = \frac{W_{\text{SOL}}}{W_{\text{tot}}}. \qquad (8)$$

Figure 6 shows the predicted fraction of power losses in the SOL ($P_{\text{abs}}$) by assuming $\nu_{\text{SOL}}/\omega = 0.01$ as a function of $n_{\text{ant}}$ for $n_\phi = -12$ and $-21$, respectively. In this figure, vertical dashed lines are the critical density ($n_{\text{ec}}$), where the FW cutoff layer is open in front of antenna.

Here, the largest SOL rectangular boundary (light blue) is the same as the one used in previous AORSA simulations, and it shows excellent agreement with Bertelli et al.[18] For $n_{\text{ant}} < n_{\text{ec}}$, when the FW cutoff layer is closed, waves are localized near the antenna and cannot propagate into the SOL. As a result, much less power is lost to the SOL. As soon as the FW cutoff is open (i.e., $n_{\text{ant}} \ge n_{\text{ec}}$), the waves start to propagate into the SOL and have strong standing modes, and thereby, $P_{\text{abs}}$ tends to be rapidly increased. For the smaller rectangular boundary case (blue and purple), $P_{\text{abs}}$ also shows a sudden increase for $n_{\text{ant}} > n_{\text{ec}}$; however, the maximum value of $P_{\text{abs}}$ is reduced when the SOL size is reduced. Here, one can note that the $n_{\text{ant}}$ where the maximum $P_{\text{abs}}$ occurs decreases as the SOL size decreases, i.e., the $P_{\text{abs}}$ gradient near the $n_{\text{ec}}$ becomes lower.

For hexagonal boundaries (dark red lines), even though the distance between the LCFS and the outer boundary is the same as the smallest rectangular boundary (purple line) as shown in Fig. 4, weaker standing modes appear as shown in Fig. 5 due to the geometry effect. Therefore, $P_{\text{abs}}$ becomes lower than the smallest rectangular boundary and gradually increases rather than showing $P_{\text{abs}}$ enhancement for $n_{\text{ec}} > n_{\text{ant}}$.

The results in this section suggest that the SOL power losses strongly depend on the boundary shape and size. We also show that
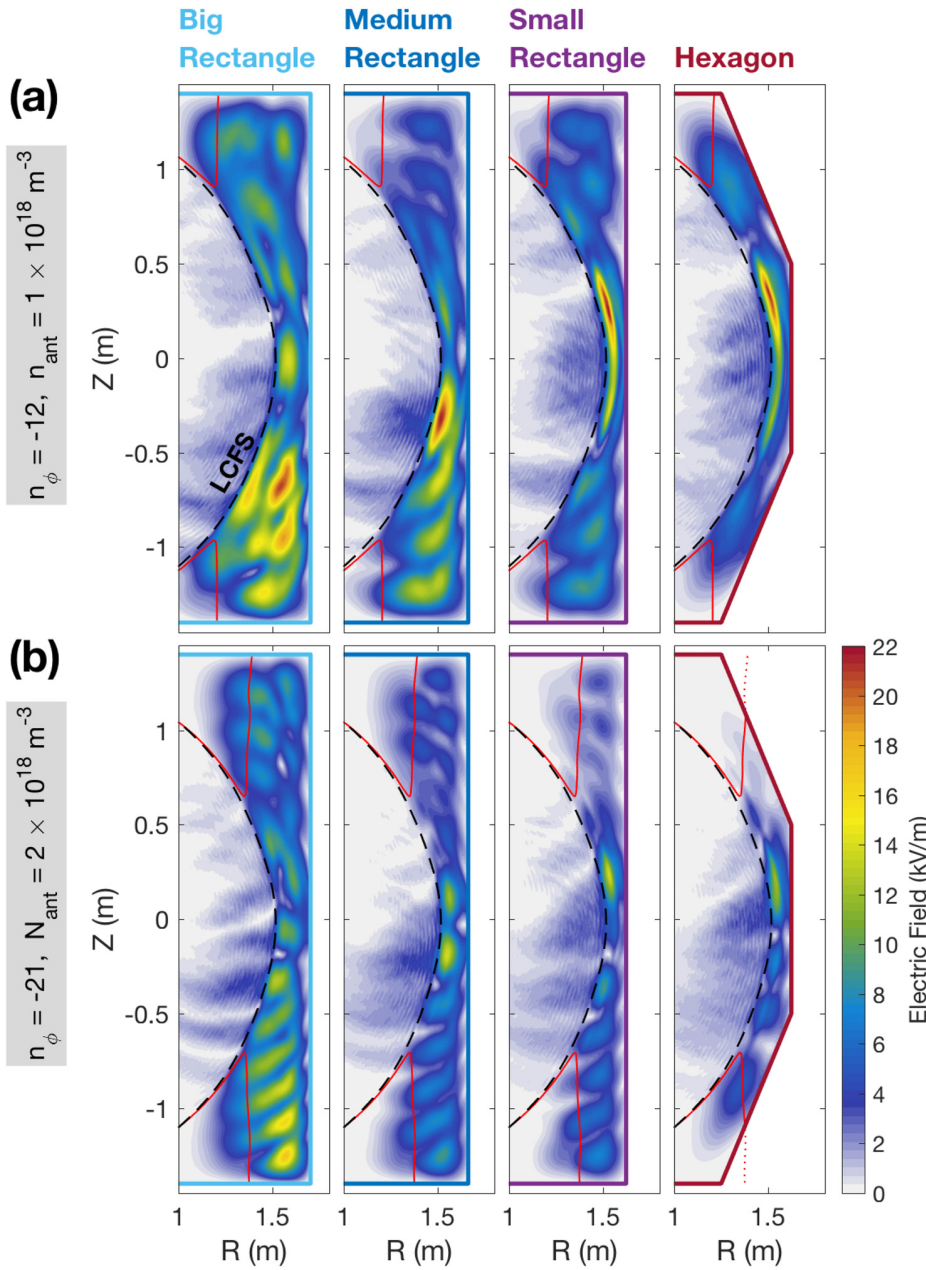
**FIG. 5.** Total electric field amplitude from the FW2D code by adopting different boundaries from left to right, big, medium, and small rectangular, and hexagonal boundaries for (a) $n_\phi = -12$ and $n_{ant} = 1 \times 10^{18}$ m$^{-3}$ and (b) $n_\phi = -21$ and $n_{ant} = 2 \times 10^{18}$ m$^{-3}$, respectively.

sudden enhancement of the power losses in the dense SOL does not occur in the non-rectangular boundary for given density range in the case of larger rectangular boundary.

### IV. HHFW WITH THE NSTX SOL BOUNDARY

In this section, we examine HHFW properties in the actual NSTX SOL boundary. We compare the wave solution with the ones using the largest rectangular SOL boundary as shown in Fig. 4. Figure 7 shows comparison of wave solutions in the NSTX-like and the rectangular SOL boundaries for $n_\phi = -21$ and $n_{ant} = 0.6$, 1.8, and

$3.0 \times 10^{18}$ m$^{-3}$. For $n_{ant} = 0.6 \times 10^{18}$ m$^{-3}$ in Fig. 7(a), the FW cutoff layer is closed, and the waves in both boundaries are almost identical. In this case, the waves are evanescent in the SOL and localized near the antenna. For $n_{ant} = 1.8 \times 10^{18}$ m$^{-3}$ in Fig. 7(b), wave solutions with two boundaries become significantly different. For the NSTX SOL boundary, even though the FW cutoff layer is open in front of the antenna, the SOL cavity of the FW mode, a region between the LCFS and the outer SOL boundary, is still very narrow and the wave power is localized near the antenna. On the other hand, waves in the rectangular boundary propagate to the SOL region and create a strong
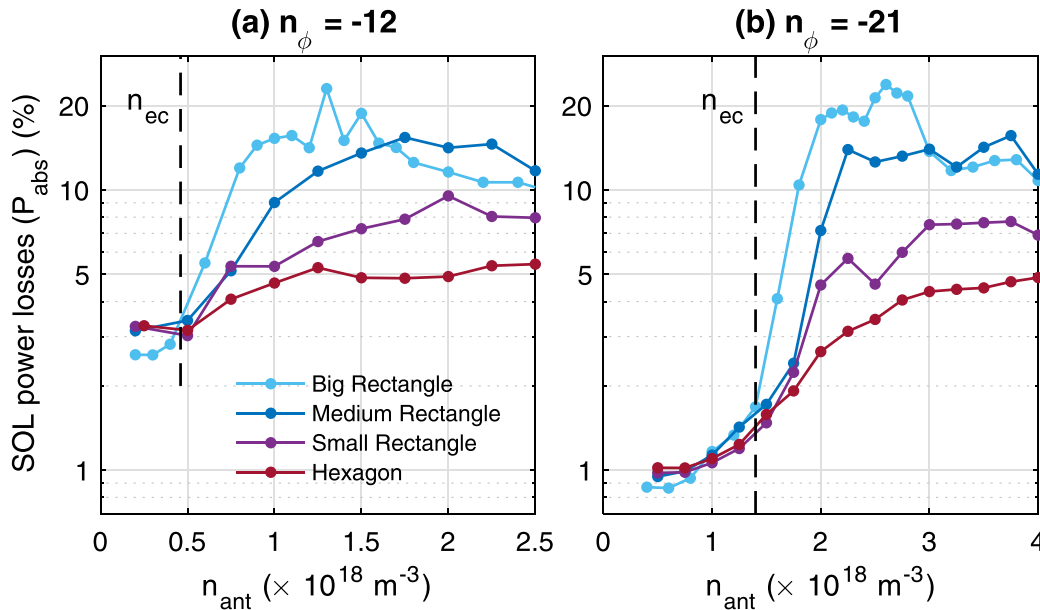
**FIG. 6.** Fraction of power lost to the SOL ($P_{abs}$) of NSTX as a function of the density in front of the antenna ($n_{ant}$) for (a) $n_\phi = -12$ and (b) $-21$ by adopting four different rectangular (light blue, blue and purple) and hexagonal (red) boundaries. The vertical lines represent the critical density ($n_{ec}$) at which the cutoff starts to be open in front of the antenna.

standing mode structure. For a higher density case of $n_{ant} = 3 \times 10^{18}$ m$^{-3}$ in Fig. 7(c), waves in the NSTX SOL boundary show the standing mode structure, but the amplitude is much weaker than the waves in the rectangular boundaries.

The same propagation behavior of the HHFW in the realistic NSTX boundary appears for different values of $n_\phi$. Figure 8 shows the total electric field amplitude for $n_\phi = -12$ when $n_{ant}$ increases from 0.4 to $3.0 \times 10^{18}$ m$^{-3}$. In this figure, amplitude of the standing mode gradually increases as $n_{ant}$ increases. When the FW cutoff layer is closed, or the SOL cavity of the FW mode is narrow as shown in Figs. 8(a)–8(c), the waves are strongly localized near the antenna and do not propagate into the SOL. Even for the dense SOL case as shown in Figs. 8(d)–8(e), the standing mode amplitudes in the NSTX boundary are not stronger than waves near the antenna, and the wave amplitude in the SOL only gradually increases as $n_{ant}$ increases.

Prior to calculating the fraction of power losses in the SOL, we examine how waves vary in the SOL for different values of collisions in the SOL. Figure 9 shows the total electric field and $\mathbf{J} \cdot \mathbf{E}*$ along $\rho_{pol} = 1.08$ marked as the red dashed line in Fig. 8(e) for $\nu_{sol}/\omega = 0.01$, 0.03, and 0.05, respectively. This figure clearly shows that $\mathbf{J} \cdot \mathbf{E}^*$ nearly linearly increases with the collision frequency in the SOL while the total electric field strength remains almost identical.

Figure 10 shows the fraction of the power losses in the SOL in the NSTX SOL boundary for $n_\phi = -12$ and $-21$ when we adopt $\nu_{sol}/\omega = 0.01$, 0.03, and 0.05. The NSTX SOL boundary is smaller than the one in the hexagonal SOL boundary as shown in Fig. 4 and it appears as the weaker standing mode in the SOL, and thus, $P_{abs}$ for $\nu_{sol}/\omega = 0.01$ is lower than that in the hexagonal boundary. As expected from the hexagonal boundary case, $P_{abs}$ gradually increases as $n_{ant}$

increases, showing consistency with the electric field configurations in Figs. 7 and 8.

Generally, we find that $P_{abs}$ in a NSTX SOL boundary is much lower than that in the rectangular boundary. Such a large amount of fraction of power losses in the rectangular boundaries is due to the geometry effect as described in Sec. III. Relatively lower power losses in the SOL can increase with the strong collisions in the SOL. As shown in Fig. 10, the $P_{abs}$ linearly increases as $\nu_{SOL}/\omega$ increases.[19] $P_{abs}$ in this case can also increase up to ∼20% for $\nu_{sol}/\omega = 0.05$ as shown in Fig. 10 and ∼40% for $\nu_{sol}/\omega = 0.15$ (not plotted here).

### A. Effect of SOL size variations

We show that the collisional power losses in the SOL are strongly affected by the SOL boundary shape and size. For better understanding power loss variations within NSTX SOL boundaries, we perform simulations by adopting various magnetic equilibriums of NSTX that has different plasma positions and thus the location of the LCFS. Figure 11(a) illustrates the outer SOL boundary and three cases of the magnetic equilibrium having different locations of the LCFS. Here, the distances between the LCFS and the outer boundary at $Z = 0$ are 11.8 cm (light blue), 9 cm (blue), and 7.2 cm (purple lines).

We then perform wave simulations by adopting various $n_{ant}$ values. Figures 11(b) and 11(c) show the calculated $P_{abs}$ from the FW2D code for $n_\phi = -12$ and $-21$, respectively. In this figure, red squares represent the critical density in front of the antenna ($n_{ec}$) in each magnetic equilibrium. Here, although the magnetic field strength is almost identical in each magnetic equilibrium, because $n_{ec}$ is proportional to the local ambient magnetic field strength,[3] $n_{ec}$ increases when the LCFS is located in the strong field side.
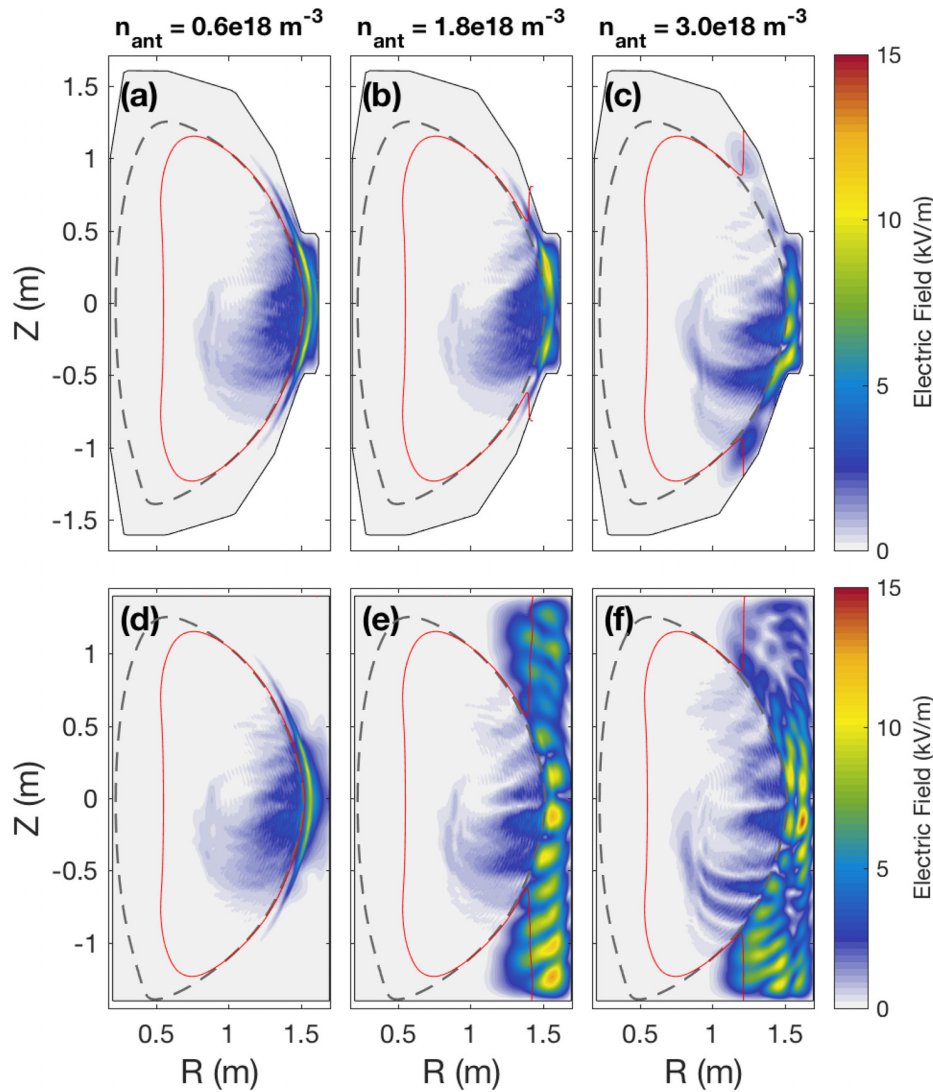
**FIG. 7.** Total electric field amplitude by adopting (a)–(c) NSTX boundary and (d)–(f) rectangular boundaries for $n_\phi = -21$ and $n_{ant} = 0.6$, $1.8$, and $3.0 \times 10^{18}$ m$^{-3}$.

Figure 11 clearly shows that stronger power losses in the SOL occur when the LCFS is located away from the antenna creating a larger SOL volume. Similar to previous cases in the SOL boundaries as shown in Fig. 10, $P_{abs}$ gradually increases as $n_{ant}$ increases. We previously show that $P_{abs}$ reaches the maximum value at higher $n_{ant}$ in the smaller SOL in Fig. 6. In order to investigate $P_{abs}$ gradient in $n_{ant}$, we also plot the differences of the power losses and the power loss at $n_{ec} = n_{ant} \left( P_{abs(n_{ant})} - P_{abs(n_{ant}=n_{ec})} \right)$ and the density in front of the antenna to the critical frequency ($n_{ant}/n_{ec}$) as shown in Figs. 11(c)–11(d). In this case, the $P_{abs}$ gradient also decreases with the decreasing SOL size.

## B. Effect of magnetic field strength

The experimental study showed that core heating in efficiency increases in the stronger magnetic field.[1–3] In this section, we investigate the effect of the magnetic field strength on the power losses in the SOL. For calculation, we adopt a H-mode scenario of NSTX-U with $B_T = 1$ T obtained by the TRANSP code[29,31] and rescale the magnetic field strength to $B_T = 0.5$ and $0.75$ T, respectively.

Figures 12(a) and 12(b) plot the $P_{abs}$ as a function of $n_{ant}$ for $n_\phi = -12$ and $-21$ and $B_T = 0.5$ (light blue), $0.75$ (blue), and $1$ T (purple). It is clear from the figure that less $P_{abs}$ occurs in the stronger magnetic field plasma, which is consistent with the experiments.[1–3]

In this figure, red squares are the critical density in front of the antenna ($n_{ec}$) in each case, showing higher $n_{ec}$ occurs in the stronger magnetic field case. For weaker magnetic field cases ($B_T = 0.5$ T), the minimum $P_{abs}$ occurs near $n_{ec}$, on the other hand, the minimum $P_{abs}$ does not occur at the $n_{ec}$ in the higher magnetic field case ($B_T = 0.75$ and $1$ T) but $P_{abs}$ gradually increase near $n_{ec}$.

A sudden increase in $P_{abs}$ occurs near $n_{ant} = 2.5$, $3.5$, and $4.5 \times 10^{18}$ m$^{-3}$ for $B_T = 0.5$, $0.75$, and $1$ T, respectively. These $P_{abs}$
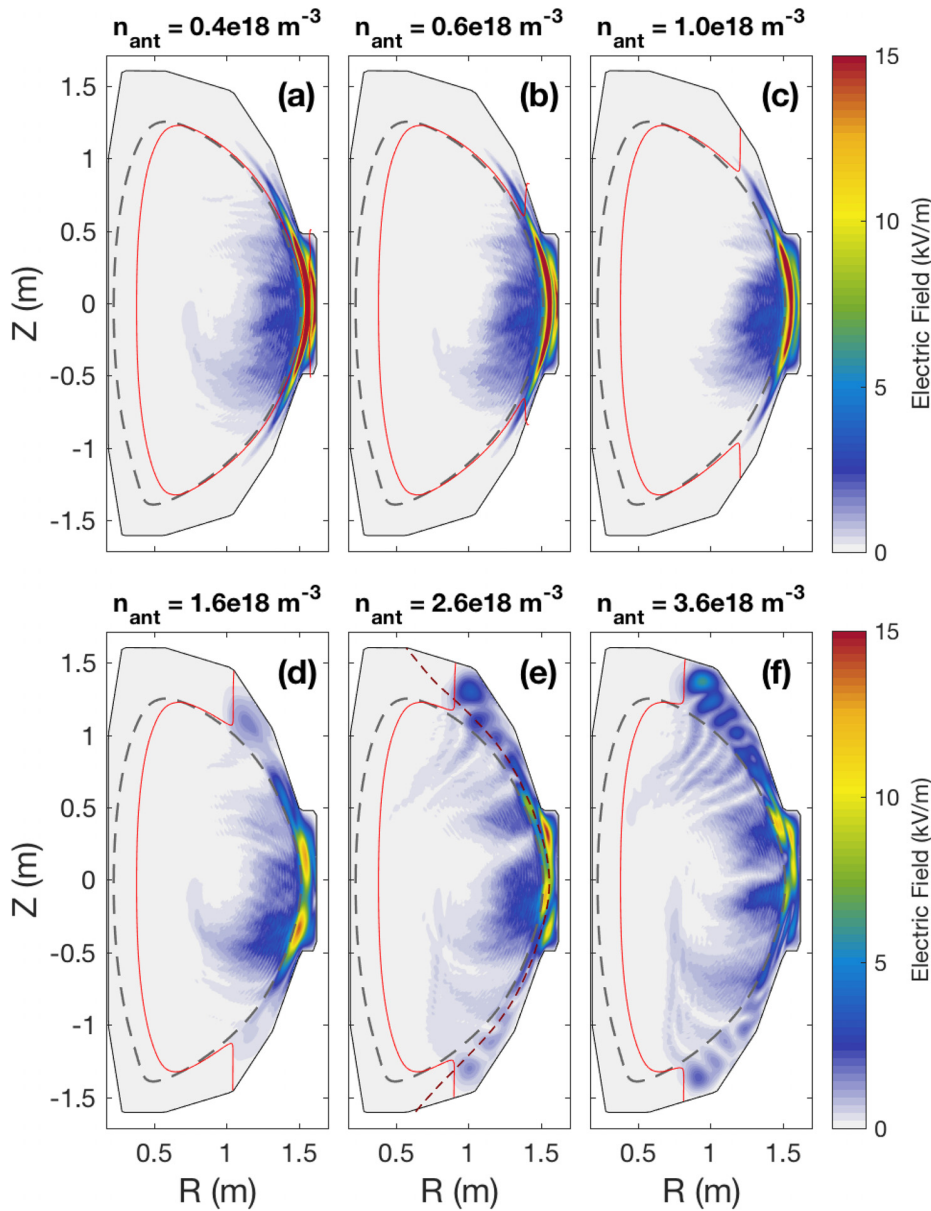
**FIG. 8.** Total electric field amplitude by adopting $n_{ant} = 0.4$–$3.6 \times 10^{18}$ m$^{-3}$ for $n_\phi = -12$ in the NSTX boundaries. The dark red dashed line in (e) is where $\rho_{pol} = 1.08$.

enhancements occur when the waves have a strong standing mode in the SOL as shown in Figs. 7 and 8. As the density in front of the antenna increases, the wavelength in the SOL decreases and the size of the SOL increases. When the SOL size is large enough to fit the wavelength, a strong standing mode and higher $P_{abs}$ occur in the SOL as shown in Fig. 12. Therefore, less power losses occur in a wide range of the $n_{ant}$ in the strongly magnetized plasma.

Figures 12(a) and 12(b) also shows that the $P_{abs}$ gradient slightly decreases as $B_T$ increases. Since $n_{ec}$ are different in each $B_T$ case, we normalized the density in front of antenna to the critical density as shown in Figs. 12(c) and 12(d). The $P_{abs}$ curves are now similar for all $B_T$ cases, suggesting the $B_T$ effects are attributable to the $n_{ec}$. Here, we

find that lower power losses in the SOL for all magnetic field strength cases occurs similar range of normalized density $n_{ant}/n_{ec}$, where $n_{ant}/n_{ec} < 2$ for $n_\phi = -12$ and $n_{ant}/n_{ec} \leq 1.25$ for $n_\phi = -21$, respectively. This result thus provides us the density range in front of the antenna where effective wave propagation into the core plasma minimizes the collisional power losses in the SOL.

## V. DISCUSSION AND SUMMARY

The NSTX experiments showed that a dramatic increase in core heating efficiency was achieved when the SOL density was lowered, and thereby, the FW cutoff is closed near the LCFS.[2,3] Thus, it has been suggested that the careful balancing of the edge density in front
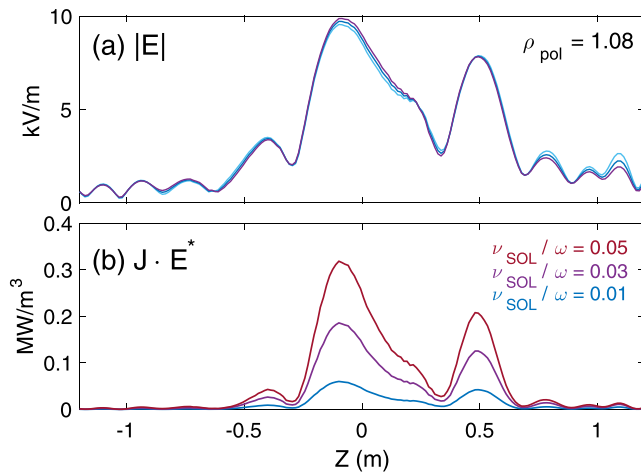
**FIG. 9.** (a) Total electric field amplitude and (b) $\mathbf{J} \cdot \mathbf{E}^*$ for $\rho_{\text{pol}} = 1.08$, $n_{\text{ant}} = 2.6 \times 10^{18}$ m$^{-3}$ and $n_\phi = -12$ in the NSTX boundaries for various collisions in the SOL, such as $\nu_{\text{SOL}}/\omega = 0.05$ (dark red), 0.03 (purple) and 0.01 (blue).

of the antenna may be required to limit edge power losses from direct fast wave damping.[3]

Previous full-wave simulations[18,19] using simplified rectangular boundaries showed a good SOL loss trend in agreement with the experiments. Enhanced power lost to the SOL occurs as soon as the FW cutoff condition in front of the antenna is open, thus the HHFW begin propagating into the SOL. Therefore, the critical density for onset of perpendicular propagation is suggested to be critical to estimate the density where strong power losses in the SOL begin, which is also confirmed by 1D wave simulations.[9] In this paper, we carried out the SOL loss calculation using a realistic NSTX SOL boundary.

In a realistic NSTX SOL boundary, we saw a simulation trend of increasing SOL losses with the SOL boundary. We see that the power losses in the SOL at the critical density have similar values to the

minimum power losses where the FW cutoff is closed, and then, the SOL power loss gradually increases as $n_{\text{ant}}$ increases as shown in Figs. 10–12. In this case, the HHFW cannot propagate to the SOL even for the FW cutoff layer in front of the antenna is open because the SOL cavity size is not enough large to maintain long wavelength FW standing modes. The SOL power losses in the NSTX SOL boundary increase gradually as the SOL density increases above the critical density as shown in Fig. 12. These results indicate that the critical density for onset perpendicular wave propagation cannot be an onset density leading large power losses in the SOL but is a critical density where the quasi-minimum SOL power losses occurs.

The experimental study also showed that large RF power loss in the SOL increases inversely with $n_\phi$ and magnetic field strength.[1–3,32] Our numerical study shows excellent agreement with the experiments. Fewer power losses in the SOL are seen in a stronger ambient magnetic field as shown in Fig. 12. It is also clearly seen that the $P_{\text{abs}}$ for $n_\phi = -21$ is higher than for $n_\phi = -12$ for the same SOL density. In addition to the lower power loss values, since the higher $n_{\text{ec}}$ appear in the strongly magnetized plasmas, it is found that lower power losses occur in a wide range of SOL density making higher $B_T$ more favorable.

We show the power losses strongly depends on the SOL boundary shape and the power losses increases as the SOL size increases. The $P_{\text{abs}}$ can increase up to $\sim$25% using the rectangular boundary[18] for $\nu_{\text{SOL}}/\omega = 0.01$. As the outer plasma LCFS boundary shifts toward antenna (thus the size of the SOL is reduced), $P_{\text{abs}}$ dramatically decreases and finally the maximum $P_{\text{abs}}$ becomes $\sim$5% for a given condition in the NSTX boundary. Compare to the experimental amount of $\sim$35% for $B_\phi = 0.55$ T, the $\sim$5% in the NSTX boundary is negligible, but the SOL absorption can increase to the experimental value of $\sim$40% when for $\nu_{\text{SOL}}/\omega = 0.15$ as shown in Fig. 10. Here, it should be noted that we adopt arbitrary collisions that represent unknown loss mechanisms in the SOL in this study. Therefore, in order to determine the dominant mechanism of power losses in the SOL, various power losses mechanism, such as surface wave propagation,[11] antenna reactive field losses,[2] or RF sheath dissipation[12–14] as well as collisions, should be considered in the future. Furthermore, in
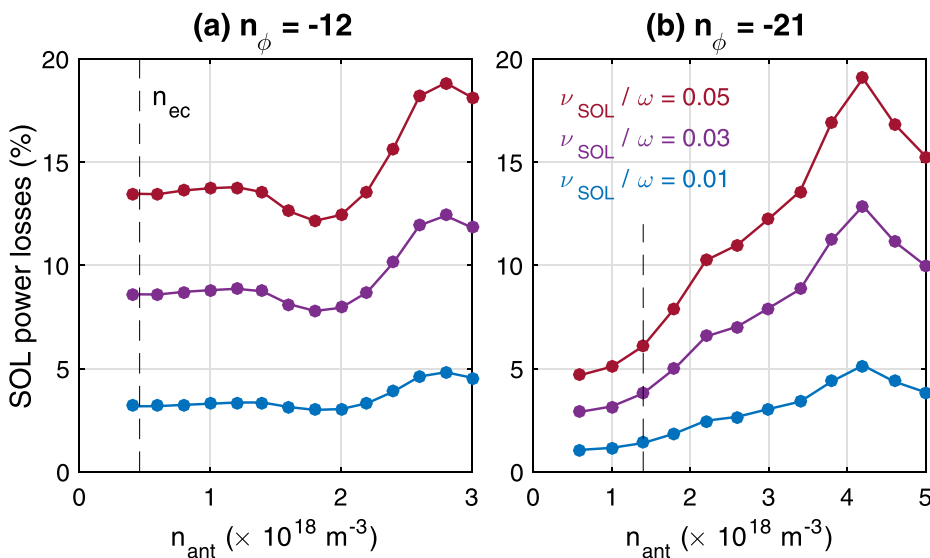


**FIG. 10.** Fraction of collisional power lost to the SOL ($P_{\text{abs}}$) of NSTX shot 130608 calculated by FW2D using NSTX boundaries as a function of the density in front of the antenna ($n_{\text{ant}}$) for (a) $n_\phi = -12$ and (b) $-21$ when various collisions in the SOL, such as $\nu_{\text{SOL}}/\omega = 0.05$ (blue), 0.03 (purple), and 0.01 (red). The vertical lines represent the critical density ($n_{\text{ec}}$) at which the cutoff starts to be open in front of the antenna.
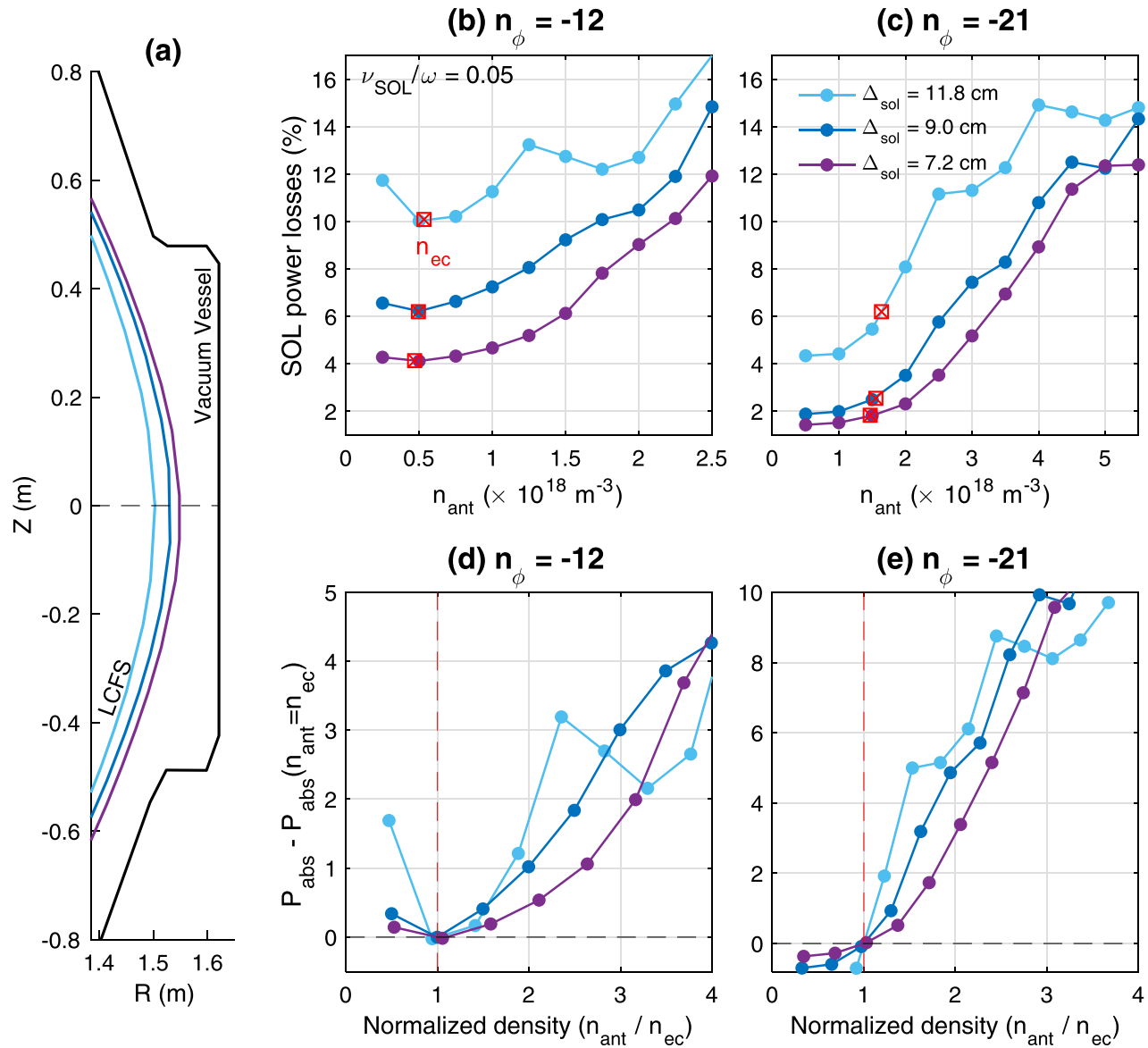
**FIG. 11.** (a) Illustration of the SOL boundary and the LCFS locations from various magnetic equilibriums. Here, the distance between the LCFS and the outer boundary at $Z = 0$ are 11.8 cm (light blue), 9 cm (blue), and 7.2 cm (purple lines). (b) and (c) Fraction of collisional power losses in the SOL ($P_{abs}$) as a function of $N_{ant}$ for different location of the LCFS for $n_\phi = -12$ and $-21$; (d) and (e) Differences between $P_{abs}$ and $P_{abs}$ where $N_{ant} = N_{ec}$ as a function of the normalized density ($n_{ant}/n_{ec}$). In this case, we assume $\nu_{SOL}/\omega = 0.05$.

order to estimate accurate collisional damping values in the SOL, realistic effective collisional frequency should be estimated from the experiments.

In summary, the effect of the wall boundary on SOL losses of HHFW in NSTX/NSTX-U is investigated using various magnetic field equilibriums with different sizes of the SOL, density in front of the antenna, and magnetic field strength. We numerically show that a realistic NSTX SOL boundary can significantly affect HHFW propagation and collisional power losses in the SOL. Because of the geometry

effect, HHFW in curval NSTX SOL boundaries less propagates to the SOL than previous simulations using rectangular boundaries, and thus, less power is lost to the SOL. The lower SOL power losses occur when SOL volume is smaller, and the distance between the last closed flux surface and the antenna is shorter. We also scan the effect of electron density in front of the antenna and the ambient magnetic field strengths on the SOL power losses in order to find the plasma condition that can minimize the SOL losses. We show that SOL losses are minimized when the SOL density is near the critical density where the
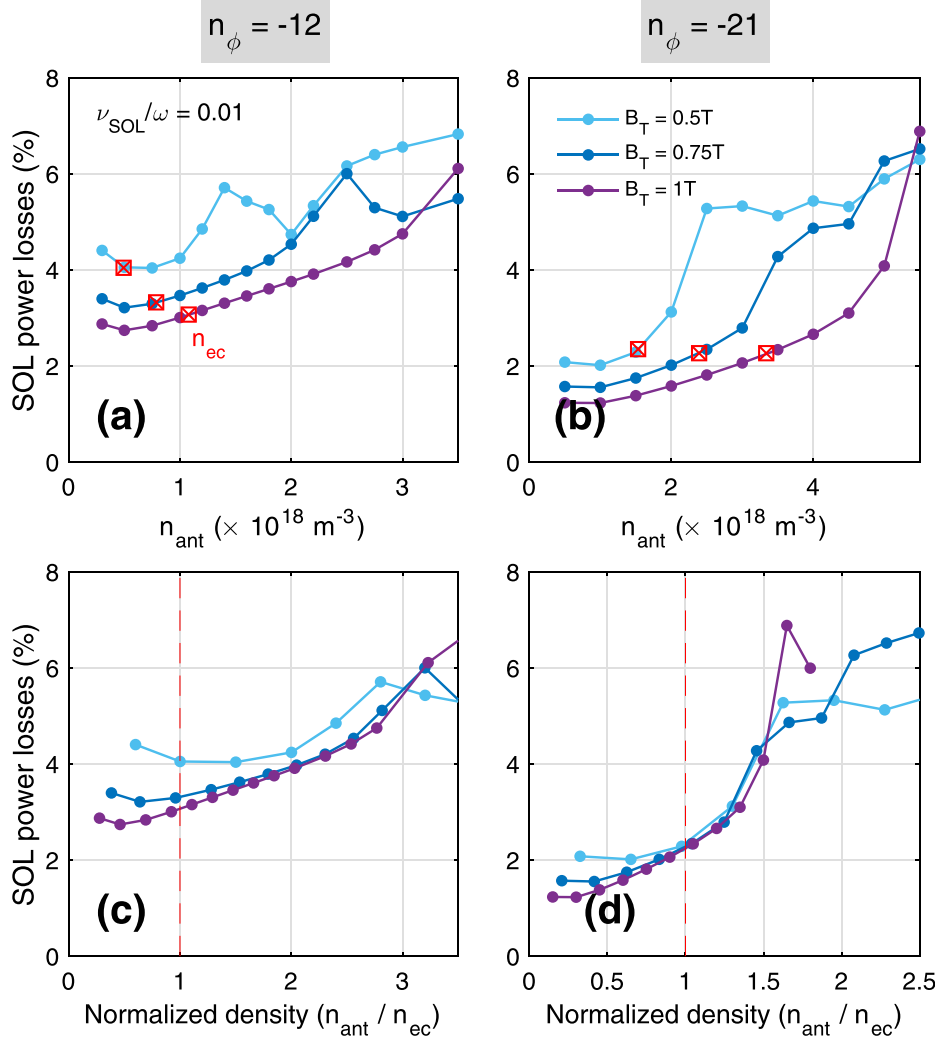
**FIG. 12.** Fraction of collisional power lost to the SOL ($P_{abs}$) of NSTX-U (a) and (b) as a function of the density in front of the antenna ($n_{ant}$) and (c) and (d) as a function of normalized density ($n_{ant}/n_{ec}$) for $n_\phi$ = −12 and −21. The light blue, blue, and purple lines represent $B_T$ = 0.5, 0.75 and 1 T, respectively. Red squares in (a) and (b) and the red vertical dashed lines in (c) and (d) are the critical density $n_{ec}$ in each magnetic equilibrium.

fast wave cutoff is open, and the plasma is strongly magnetized, which is consistent with the experiments.

## ACKNOWLEDGMENTS

## REFERENCES

[1]J. Hosea, S. Bernabei, T. Biewer, B. Leblanc, C. K. Phillips, J. R. Wilson, D. Stutman, P. Ryan, and D. W. Swain, in *Proceedings of 16th Topical Conference on Radio-Frequency Power in Plasmas* (AIP Conference Proceedings, New York, 2005), pp. 82–85.

[2]J. Hosea, R. E. Bell, B. P. LeBlanc, C. K. Phillips, G. Taylor, E. Valeo, J. R. Wilson, E. F. Jaeger, P. M. Ryan, J. Wilgen *et al.*, Phys. Plasmas **15**, 056104 (2008).

[3]C. Phillips, R. Bell, L. Berry, P. Bonoli, R. Harvey, J. Hosea, E. Jaeger, B. LeBlanc, P. Ryan, G. Taylor *et al.*, Nucl. Fusion **49**, 075015 (2009).

[4]G. Taylor, R. E. Bell, J. C. Hosea, B. P. LeBlanc, C. K. Phillips, M. Podesta, E. J. Valeo, J. R. Wilson, J.-W. Ahn, G. Chen *et al.*, Phys. Plasmas **17**, 056114 (2010).

[5]R. J. Perkins, J. C. Hosea, G. J. Kramer, J.-W. Ahn, R. E. Bell, A. Diallo, S. Gerhardt, T. K. Gray, D. L. Green, E. F. Jaeger *et al.*, Phys. Rev. Lett. **109**, 045001 (2012).

[6]R. Perkins, J.-W. Ahn, R. Bell, A. Diallo, S. Gerhardt, T. Gray, D. Green, E. Jaeger, J. Hosea, M. Jaworski *et al.*, Nucl. Fusion **53**, 083025 (2013).

[7]M. Ono, S. Kaye, Y.-K. Peng, G. Barnes, W. Blanchard, M. Cartera, J. Chrzanowski, L. Dudek, R. Ewigb, D. Gates *et al.*, Nucl. Fusion **40**, 557 (2000).

[8]S. Kaye, T. Abrams, J.-W. Ahn, J. Allain, R. Andre, D. Andruczyk, R. Barchfeld, D. Battaglia, A. Bhattacharjee, F. Bedoya *et al.*, Nucl. Fusion **55**, 104002 (2015).

[9]R. Perkins, J. C. Hosea, N. Bertelli, G. Taylor, and J. R. Wilson, Nucl. Fusion **57**, 116062 (2017).

[10]T. H. Stix, *Waves in Plasmas* (American Institute of Physics, New York, 1992).

[11]P. Colestock, G. J. Greene, J. C. Hosea, C. K. Phillips, J. E. Stevens, M. Ono, and J. R. Wilson, Fusion Eng. Des. **12**, 43 (1990).

[12]J. M. Noterdaeme and G. V. Oost, Plasma Phys. Controlled Fusion **35**, 1481–1511 (1993).

[13]J. R. Myra, D. A. D'Ippolito, D. A. Russell, and L. A. Berry, in *Proceedings of the 16th Topical Conference on Radio-Frequency Power in Plasmas* (AIP Conference Proceeding, New York, 2005), pp. 3–14.

[14]L. Colas, E. Faudot, S. Br'emond, S. Heuraux, R. Mitteau, M. Chantant, M. Goniche, V. Basiuk, G. Bosia, J. P. Gunn *et al.*, *Proceedings of the 16th Topical Conference on RF Power in Plasmas* (AIP Conference Proceeding, New York, 2005), pp. 150–157.

[15]E. F. Jaeger, L. A. Berry, E. DAzevedo, D. B. Batchelor, and M. D. Carter, Phys. Plasma **8**, 1573 (2001).

[16]J. Menard, J. Allain, D. Battaglia, F. Bedoya, R. Bell, E. Belova, J. Berkery, M. Boyer, N. Crocker, A. Diallo *et al.*, Nucl. Fusion **57**, 102006 (2017).

[17]D. L. Green, L. A. Berry, G. Chen, P. M. Ryan, J. M. Canik, and E. F. Jaeger, Phys. Rev. Lett. **107**, 145001 (2011).

[18]N. Bertelli, E. Jaeger, J. Hosea1, C. Phillips, L. Berry, S. Gerhardt1, D. Green, B. LeBlanc, R. Perkins, P. Ryan *et al.*, Nucl. Fusion **54**, 083004 (2014).

[19]N. Bertelli, E. Jaeger, J. Hosea, C. Phillips, L. Berry, P. Bonoli, S. Gerhardt, D. Green, B. LeBlanc, R. Perkins *et al.*, Nucl. Fusion **56**, 016019 (2016).

[20]D.-H. Lee and R. L. Lysak, J. Geophys. Res. **94**, 17097, https://doi.org/10.1029/JA094iA12p17097 (1989).

[21]E.-H. Kim, J. R. Johnson, E. Valeo, and C. K. Phillips, Geophys. Res. Lett. **42**, 5147, https://doi.org/10.1002/2015GL064531 (2015).

[22]E.-H. Kim and J. R. Johnson, Geophys. Res. Lett. **43**(1), 13–21, https://doi.org/10.1002/2015GL066978 (2016).

[23]E.-H. Kim, N. Bertelli, E. Valeo, J. Hosea, R. Perkins, and J. R. Johnson, EPJ Web Conf. **157**, 02005 (2017).

[24]M. Brambilla, Plasma Phys. Controlled Fusion **41**, 1 (1999).

[25]N. E. Gibbs, W. G. J. Poole, and P. K. Stockmeyer, SIAM J. Numer. Anal. **13**, 236–250 (1976).

[26]P.-O. Persson and G. Strang, SIAM Rev. **46**, 329 (2004).

[27]J. R. Shewchuk, Comput. Geom. **22**, 21 (2002).

[28]E. F. Jaeger, L. A. Berry, J. R. Myra, D. B. Batchelor, E. D'Azevedo, P. T. Bonoli, C. K. Phillips, D. N. Smithe, D. A. D'Ippolito, M. D. Carter *et al.*, Phys. Rev. Lett. **90**, 195001 (2003).

[29]N. Bertelli, E. Jaeger, L. Berry, P. T. Bonoli, R. Budny, F. G.-Y, S. Gerhardt, D. L. Green, R. W. Harvey, J. C. Hosea *et al.*, AIP Conf. Proc. **1580**, 310 (2014).

[30]C. Lau, F. Jaeger, N. Bertelli, L. Berry, D. L. Green, M. Murakami, J. M. Park, R. I. Pinsker, and R. Prater, Nucl. Fusion **58**, 066004 (2018).

[31]S. Gerhardt, R. Andre, and J. Menard, Nucl. Fusion **52**, 083020 (2012).

[32]J. Hosea and PPPL ICRF Teams, EPJ Web Conf. **157**, 02003 (2017).